Interfacial Carbon Makes Nano-Particulate RuO_2 an Efficient, Stable, pH-Universal Catalyst for Splitting of Seawater

Fang Fang, Yong Wang, Le-Wei Shen, Ge Tian, David Cahen, Yu-Xuan Xiao, Jiang-Bo Chen, Si-Ming Wu, Liang He, Kenneth I. Ozoemena, Mark D. Symes and Xiao-Yu Yang**

F. Fang, Y. Wang, L.-W. Shen, Dr. G. Tian, Y.-X. Xiao, J.-B. Chen, S.-M. Wu, Prof. L. He, Prof. X.-Y. Yang
State Key Laboratory of Advanced Technology for Materials Synthesis and Processing & School of Materials Science and Engineering & International School of Materials Science and Engineering & Shenzhen Research Institute & Joint Laboratory for Marine Advanced Materials in Pilot National Laboratory for Marine Science and Technology (Qingdao), Wuhan University of Technology, Wuhan, 430070, China. E-mail: xyyang@whut.edu.cn; tiange@whut.edu.cn

Prof. D. Cahen
Dept. of Chemistry, and Bar-Ilan Inst. for Nanotechnol. & Adv. Mater. (BINA), Bar-Ilan University, Ramat Gan, Israel 5290002 (also at Weizmann Inst. of Science, Rehovot Israel 76100)

Prof. K. I. Ozoemena
Molecular Sciences Institute, School of Chemistry, University of the Witwatersrand, Private Bag 3, Johannesburg 2050, South Africa.

Prof. M. D. Symes
WestCHEM, School of Chemistry, University of Glasgow, University Avenue, Glasgow, G12 8QQ, UK.

Keywords: hierarchical nanostructure, directed transformation, seawater splitting, RuO_2-based electrocatalysts, interface engineering

Abstract

An electrocatalyst composed of RuO_2 surrounded by interfacial carbon, was synthesized through controllable oxidization-calcination. This electrocatalyst provides efficient charge transfer, numerous active sites, and promising activity for pH-universal electrocatalytic overall

seawater splitting. An electrolyzer with this catalyst gave current densities of 10 mA cm^{-2} at a record low cell voltage of 1.52 V, and shows excellent durability at current densities of 10 mA cm^{-2} for up to 100 h. Based on the results a mechanism for the catalytic activity of the composite is proposed. Finally, a solar-driven system was assembled and used for overall seawater splitting, showing 95% Faraday efficiency.

1. Introduction

Renewable energy-driven electrocatalytic water splitting is seen as a promising route for the sustainable production of H_2 as a fuel, e.g., for fuel cells. The oceans represent a vast reservoir of water as input material for such H_2 production.[1-3] However, the high salinity and compositional complexity of seawater presents challenges in terms of electrocatalyst deactivation and undesirable side reactions.[4-6] Ruthenium dioxide (RuO_2) displays good corrosion resistance towards seawater and its electrocatalytic performance for the hydrogen and oxygen evolution reactions (the HER and OER) is very attractive.[7-9] There have been a number of successful approaches for further improvement of the electrocatalytic activity of RuO_2, such as particle nanosizing, morphological control, crystal amorphization, facet adjustments, engineering of vacancies, introduction of impurities and so on.[10-18] Notably, because of oxygen vacancies in RuO_2 (and the resultant exposure of surface Ru species), use of RuO_2 as an anode in high salinity systems such as seawater can lead to the deactivation of RuO_2 by the adsorption of various ions and subsequent over-oxidation to soluble Ru oxides such as RuO_4.[15,19,20] This Ru corrosion during seawater splitting unavoidably leads to the faster collapse of the crystal structure than is the case if less saline electrolytes are used.[19] Unfortunately, detailed reports on the stability of RuO_2 in seawater are very rare. Considering the use of RuO_2 for overall seawater splitting, the design of current electrolyzers is not optimal because the most appropriate operating conditions for the HER and OER are often not the same.[8,21,22] For example, the HER is generally easier to perform in acidic than in alkaline solutions, because in acidic environment protons (H^+) can combine directly with an electron, forming H^* and then H_2, while for the OER in alkaline solution OH^- ions enable the direct formation of HO^*, which then proceeds through further intermediates to give O_2 as the product.[8,23,24] The challenge is therefore to develop pH-universal RuO_2 electrocatalysts for practical overall seawater splitting.[8] Such a RuO_2 electrocatalyst will allow for efficient catalysis of both the HER and OER in the same medium, which will not only make electrolyzer assembly easier, but also solve the catalyst dissolution-redeposition problem, which often occurs if different catalysts are used for the HER and OER.

Considering the above-mentioned application of RuO_2 to seawater splitting, catalyst stability under high salinity and across all pH conditions with reasonable overall catalytic efficiency is required. Carbon has been widely used in electrocatalyst design as an efficient electron transfer medium and support for catalyst dispersion. Very interestingly, carbon also shows high chemical resistance to seawater, acids and alkalis, and so could be ideal as catalyst support for electrocatalytic overall seawater splitting.[25,26] For example, graphene, as a surface coating or support for RuO_2, has been used for both the HER and OER half reactions, in spite of the synthetic complexity involved in its preparation. Carbonization by high-temperature calcination in an inert atmosphere is a common method by which to fabricate Ru/C species; however, it inevitably forms surface carbon deposits that often cover the active sites of RuO_2.[27] An ideal RuO_2/C structure would consist of RuO_2 nanocrystals surrounded only by interfacial carbon, which would not only give a maximum number of exposed (Ru) sites, but also combine the advantageous features of efficient electron transfer and high catalyst dispersion. Moreover, high-efficiency OER activity will minimize the chlorine evolution reaction (ClER). Most recently, a facial direct-oxidation calcination method that we developed has been used to precisely control the homogeneous distribution of carbon in semiconductor/carbon compositions for efficient carrier utilization and excellent electrocatalytic performances.[28,29]

Here we report that nanosized RuO_2 with interfacial C is as an effective electrocatalyst for pH-universal overall seawater splitting via confinement ion-exchange (Cu^{2+} replaced by Ru^{3+}) in the microporous, metal-organic framework compound copper benzene-1,3,5-tricarboxylate (Cu-BTC), by solvothermal treatment, followed by controlled oxidization by calcination. The remarkable activity of the RuO_2/C catalyst is traced to its morphology and surface chemical composition, both the result of the preparation conditions. A solar-driven version of the electrocatalytic system with 95% Faraday efficiency was demonstrated for overall seawater splitting.

2. Results and Discussion

To optimize the design and synthesis of nanostructured RuO_2-based catalysts, thermogravimetric and differential scanning calorimetry analyses (TG-DSC) (**Figure 1a**) were used to optimize the calcination temperature for the transformation of the precursor Ru^{3+}-C into the catalyst. The content of Cu in the ion-exchange derived Ru^{3+}-C has been determined to be very low. The atomic ratio of Ru:Cu is found to be about 82:1 using an energy-dispersive X-ray spectroscopy (EDS) test (Table S1), and the ratio decreases to be about 21:1 using an inductively coupled plasma-atomic emission spectroscopy (ICP) test (Table S1). This is

because that RuO_2 is difficult to be dissolved in aqua regia, which can lead to relatively lower ratio of Ru:Cu detected by ICP test. The first mass loss of 10 wt.% in the temperature range from 100 °C to 180 °C (see TGA trace) can be ascribed to loss of surface-absorbed water, and the second sharp one of 51 wt.% between 190 °C and 380 °C (TGA) can be assigned to the thermal decomposition of the organic framework. Note that the exothermic DSC peak of Ru^{3+}-C in the range of decomposition of the organic framework includes two features, one between 190 °C and 310 °C and the other between 310 °C and 380 °C. A logical interpretation is that surface carbon species are removed first (as they react most easily with oxygen), and that then the inner carbon species in between the RuO_2 nanoparticles are removed at a decreasing rate when increasing the temperature from 310 °C to 380 °C. The DTG curve reveals that there is a very sharp maximum in the rate of weight loss at 310 °C, which makes it hard to control the remaining carbon content. Based on our interpretation that heating till 310 °C leaves the inner carbon between the Ru-oxide grains intact, we selected 300 °C as calcination temperature.

Powder X-ray diffraction (XRD) provides further justification for this choice, because, as shown in Figure 1b, clear diffraction peaks start to appear, superimposed on a broad feature, only at 300 °C; with increasing calcination temperature these peaks become clearer until only they remain. The diffraction peaks at 28.01°, 35.05° and 54.25° can be assigned to the (110), (101) and (211) planes of RuO_2 with tetragonal phase (ICDD no. 01-070-2662), respectively. The broad diffraction peaks of RuO_2-C-300 indicate that the RuO_2 grains are small. These changes can be also seen in the Fourier transform infrared (FT-IR) spectra (Figure S1),[30] which show that almost all the prominent organic functional groups' peaks disappear after calcination at 300 °C. And morphology of samples have been observed by scanning electron microscopy (SEM), which shows that ion-exchange process and calcination can lead to size shrinkage of the particles, while the morphology does not change much with temperature from 250 °C to 400 °C (Figure S2).

As shown in Figure S3, the 290-280 eV binding energy (BE) range of the XPS data could be fit to 2 sets of Ru 3d doublets and two organic C1s ones, in total six peaks. An interesting difference in Ru3d BEs between the RuO_2-C-250 sample, on the one hand, and the RuO_2-C-300, RuO_2-C-350, and RuO_2-C-400 ones on the other hand (Figure 1c), which is due to the presence of unoxidized Ru^{3+}, which could not be oxidized at the lowest calcination temperature. The Ru 3d BE for RuO_2-C-300 is still somewhat affected by that of the less crystalline phase. [31] Moreover, the high-resolution O 1s spectra of the above four samples can be deconvoluted into four different oxygen species, namely the lattice O of RuO_2 and those in Ru-OH, C=O and absorbed H_2O (Figure 1d).[32,33] As the temperature increases, the hydroxyl content in the

material decreases and the oxide content increases. In summary, TGA-DSC, FT-IR, XRD and XPS results indicate that calcination at 300°C or higher temperatures leads to formation of RuO_2, containing C and OH groups.

In order to analyze the surface area of our samples, critical for catalytic activity, at different calcination temperatures, N_2 adsorption-desorption isotherms were measured (Figure S4). We find that RuO_2-C-300 still shows a packing-aggregation mesostructured with a pore size of 3.5 nm (Figure S4b) and a Brunauer-Emmett-Teller (BET) surface area of 76 cm^2 g^{-1} (Table S2). With increasing calcination temperature, the small pores of Ru^{3+}-C disappear first and then the larger mesopores of RuO_2-C-280 become 3.8 nm mesopores (Table S2). This change suggests that the original porous structure of the organic framework collapses and pores form between the RuO_2 nanoparticles. Considering that the pore sizes of the RuO_2-C-300, RuO_2-C-350 and RuO_2-C-400 are found to be the same (~ 3.5 nm), and that also after calcination at 300°C there is still carbon in the samples, as indicated by esp., infra-red spectroscopy, we conclude that the remaining carbon is interfacial between the RuO_2 particles, rather than at the surface, where it would block the pores.[34]

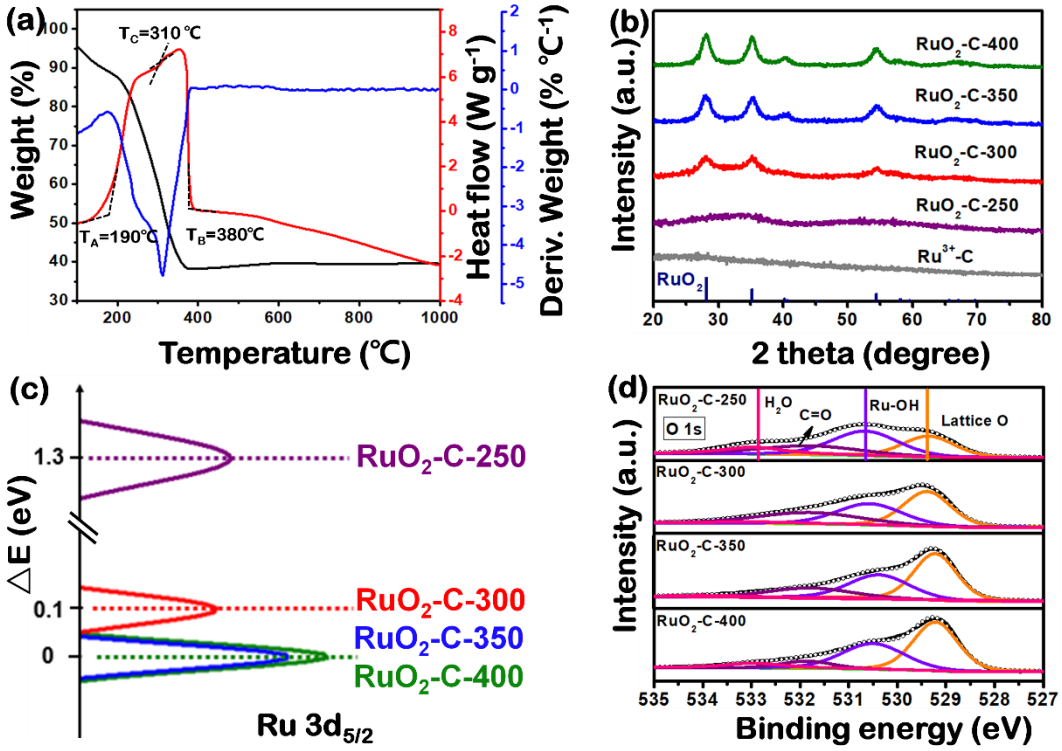

Figure 1. Effects of different calcination conditions, from 250 °C to 400 °C for 4 h, used to synthesize the RuO_2-based electrocatalysts (denoted as RuO_2-C-T, where T is 250, 300, 350 and 400) (a) TG-DSC analysis of as-prepared Ru^{3+}-C, in air. (b) XRD patterns of as prepared Ru^{3+}-C, RuO_2-C-250, RuO_2-C-300, RuO_2-C-350, RuO_2-C-400. (c) Ru $3d_{5/2}$ XPS peak shift in

Ru^{3+}-C, RuO_2-C-250, RuO_2-C-300, RuO_2-C-350, with respect of the Ru $3d_{5/2}$ line in RuO_2-C-400. (d) XPS O 1s spectra of RuO_2-C-300.

To try to get a direct nm-scale view of the optimized, RuO_2-C-300 samples, their structure and morphology were investigated by transmission electron microscopy (TEM) and high-angle annular dark-field scanning transmission electron microscopy (HAADF-STEM). As can be seen in Figure 2a, RuO_2-C-300 is composed of polyhedral particles with uniform size of around 400 nm, each of these particles is composed of smaller nanoparticles. Elemental mapping, using energy-dispersive X-ray spectroscopy, EDS (Figure 2b) indicates a homogeneous distribution of Ru, O and C, suggesting that the carbon is uniformly retained. High-resolution TEM (HRTEM) imaging (Figure 2c, S5, S6) shows that ultra-small crystalline nanoparticles (yellow) with sizes 5-20 nm are dispersed and surrounded by an amorphous (blue) structure. The lattice spacing of the nanoparticles is measured to be about 0.32 or 0.25 nm, corresponding to the (110) or (101) interplane distances of the rutile structure of RuO_2, respectively. Evidence of lattice fusion of RuO_2 nanoparticles is observed in the inverse FFT images of the regions I from Figure 2c (Figure 2d; magnified in Figure 2e).

Because at a calcination temperature of 300 °C it is impossible to convert the amorphous carbon species to graphitic carbon, we suggest that the amorphous regions result from fusion of interfacial carbon and low crystallinity RuO_2 and is limited to a few nm. In the precursor, the Ru^{3+} ions are coordinated by carboxylate oxygen atoms. During the controlled oxidization by calcination, Ru^{3+} ions are gradually oxidized and sintered to small RuO_2 nanoparticles with low crystallinity. Most of the ligands will be oxidized to CO_2 gases, while partial ligands surrounded by RuO_2 nanoparticles will be carbonized to form interfacial carbon. It is possibly that some of the interaction of Ru-O-C may be preserved in the RuO_2-carbon composite, which lead to the fusion between interfacial carbon and low crystallinity RuO_2. This nano-scale fusion binds the RuO_2 nanocrystals, which helps exposing more active sites and also stabilizes the nanoparticles. The fact that the RuO_2 particles are separated by only 0.5-2.5 nm allows efficient electron tunnelling at ~10 mA cm^{-2} current densities; thus, the interfacial carbon layer can mediate efficient charge transfer between the RuO_2.[34,35] In the selected area electron diffraction (SAED) pattern, two continuous diffraction rings are seen, which can be indexed to the (101) and(211) planes of rutile-type RuO_2 (Figure 2f). The width of the rings can be attributed to the small particle size and low crystallinity of RuO_2.[36,37]

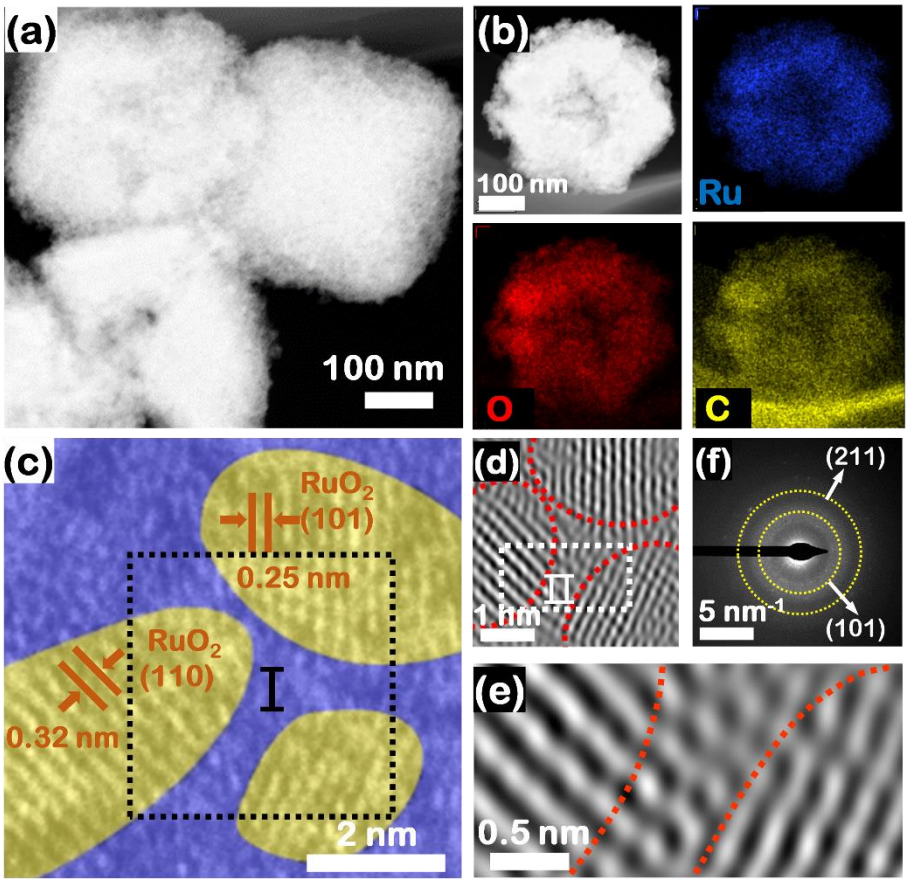

Figure 2. Morphologies and structures of RuO_2-C-300. (a) High-Angle Annular Dark Field (HAADF) STEM image. (b) Top left: HAADF-STEM image; other images are EDS elemental maps (Ru: blue, O: red, C: yellow). (c) Artificially coloured version of the HRTEM image, shown in Figure S6: two different colours are used to distinguish the crystalline (yellow) and amorphous (blue) regions. (d) Inverse FFT image of region I from panel c, showing the crystal fusion region between the RuO_2 nanoparticles. (e) Magnified image of region II from panel (d). (f) Selected area electron diffraction (SAED) pattern from area shown in Figure S5; it is based on the raw SEAD pattern, shown in Figure S7.

The effects of these features are evident in the electrocatalytic HER and OER. For example, in N_2-saturated 1 M KOH solution, RuO_2-C-300 exhibits excellent performance in terms of overpotential (@ 10 mA cm^{-2}) for both the HER (18 mV) and OER (246 mV), when compared with Pt/C (48 mV for the HER) and commercial RuO_2 (368 mV for the OER) (Figure S8, Table S3). All overpotential metrics reported herein were collected at least twice and are accurate to within ±10%. Similar excellent performances of RuO_2-C-300 can be seen in acidic electrolyte (Figure S9, Table S3). Also, for overall water splitting, the RuO_2-C-300 electrodes show good performance and stability in 1 M KOH electrolyte (initial 1.5 V @10 mA cm^{-2} and increasing to 1.58 V after 20 h, Figure S10). It is suggested that the contribution of remaining Cu to

performances can be excluded although traces of Cu has been detected (Table S1). Because the samples obtained through calcination at different temperatures were all from the same precursor, the atomic ratios of Ru:Cu are assumed to be similar in all these samples, while their performances vary greatly.

To assess the potential of RuO_2-C-300 for overall seawater splitting, its electrocatalytic HER and OER performance should be compared to those of commercial Pt/C (comm-Pt/C), and commercial RuO_2-carbon mixture (comm-RuO_2/C) catalysts in alkaline, neutral and acidic simulated (standard 3.5 wt.% NaCl solution) and natural seawater electrolytes, giving 6 types of electrolytes as follows: 1 M KOH+simulated seawater ("alkaline sS"), 1 M KOH+natural seawater ("alkaline nS"), 1 M PBS buffer+simulated seawater (" neutral sS") and 1 M PBS buffer+natural seawater (" neutral nS"), 0.5 M H_2SO_4+simulated seawater ("acidic sS") and 0.5 M H_2SO_4+natural seawater (" acidic nS").

As shown in Figures 3a-c and Table S4, in simulated seawater electrolytes, RuO_2-C-300 shows excellent performances with very small HER and OER overpotentials of only 27 and 346 mV required under alkaline conditions (Figure 3a), 94 and 370 mV under neutral conditions (Figure 3b), and 92 mV and 150 mV under acidic conditions (Figure 3c), respectively. The relatively low OER overpotential requirement that is observed in acidic solution might be due to competing chlorine evolution, which is known to have a relatively low overpotential requirement under acidic conditions. In the natural seawater electrolytes (Figure 3d-f), the HER and OER overpotentials for RuO_2-C-300 at 10 mA cm^{-2} are only 15 mV and 270 mV under alkaline conditions (Figure 3d), 56 mV and 320 mV under neutral conditions (Figure 3e), and 121 mV and 198 mV under acidic conditions (Figure 3f), respectively. With the exception of the HER activity of Pt/C in acidic solution, all these performances are superior to those obtained with Pt/C and commercial RuO_2/C catalysts.

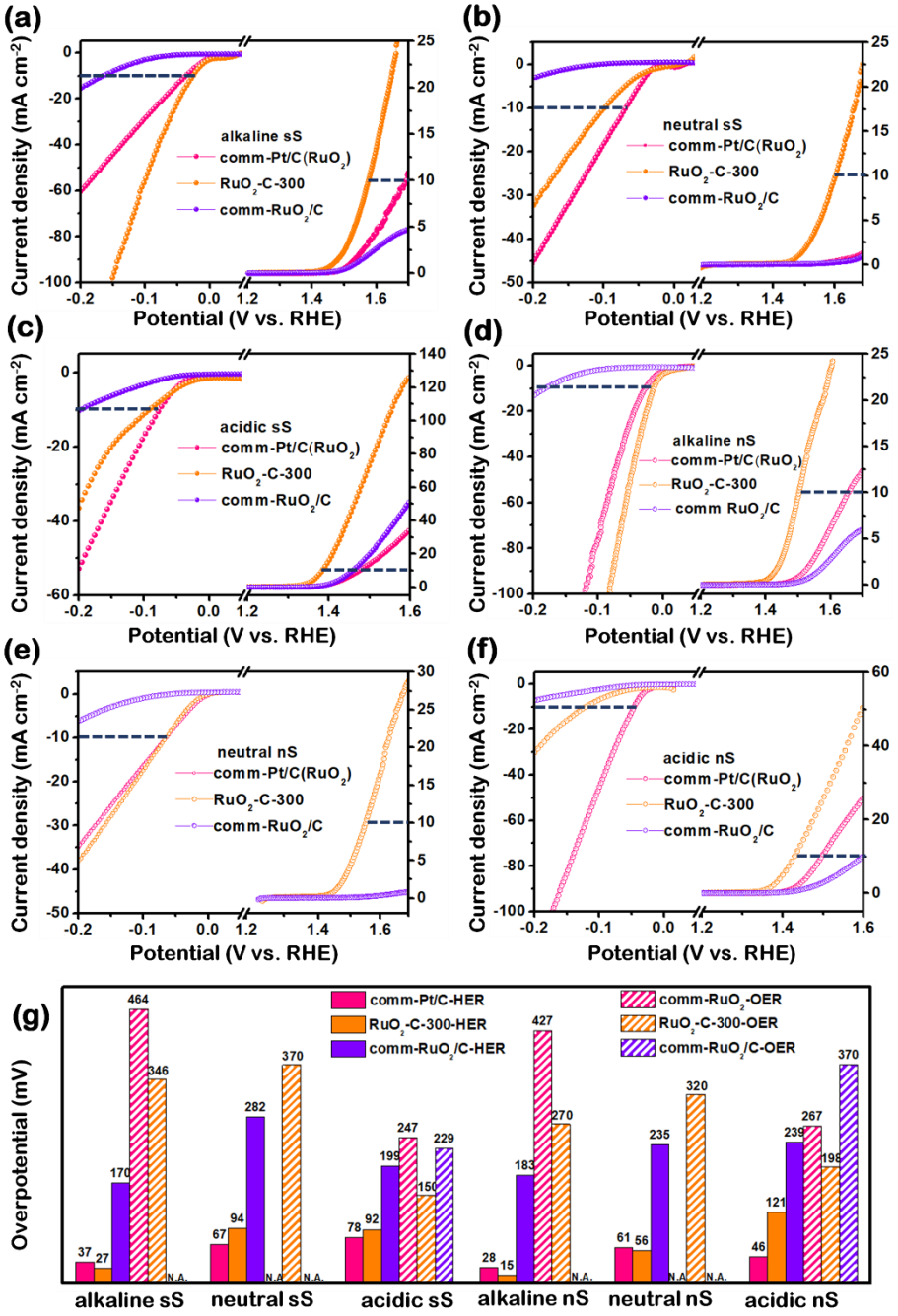

Figure 3. (a-f) HER (left) and OER (right) polarization curves of RuO_2-C-300, commercial Pt/C, and comm-RuO_2/C in alkaline sS and alkaline nS, neutral sS and neutral nS, acidic sS and acidic nS. (g) Comparison of HER and OER overpotentials @10 mA cm^{-2} in different electrolytes. The numbers at the top of the bars are in mV.

It is worth to note that the electrocatalytic activity of RuO_2-C-300, in either simulated or natural seawater, is hardly changed in comparison with that in non-saline water, but the Pt/C and commercial RuO_2 both show a relatively large decrease in their activities under almost all the conditions tested, relative to that in non-saline water. Probably, the high salinity (and complex composition of natural seawater) are the main reasons for this deactivation of the

conventional catalysts, but RuO_2-C-300 samples have the advantage of being highly-resistant to seawater corrosion. The commercial RuO_2/C shows very poor activity for HER and OER in all conditions, which is attributed to a decrease in the number of exposed active sites of the catalyst and low affinity to water, due to carbon coverage of the RuO_2/C catalyst (Figure S11 and S12).

Given the excellent catalytic performance of RuO_2-C-300 in alkaline natural seawater electrolyte, RuO_2-C-300 was integrated into a two-electrode system with that electrolyte, to investigate overall seawater splitting performance. In this setup, RuO_2-C-300 showed excellent activity for overall seawater splitting in alkaline natural seawater electrolyte, with voltage of 1.52 V to obtain current density of 10 mA cm^{-2} and runs for 100 hours without obvious decay (Figure 4a, 4b). The leaching of RuO_2 is detected to be very little (~0.7 wt. %, 2.6 μmol L^{-1} of Ru cations from ICP-AES data). The overall seawater splitting performance of RuO_2-C-300 is better than, or similar to that of other reported excellent performance catalysts (Table S5). It is possibly for the Ca^{2+} and Mg^{2+} ions in seawater to deposit on cathode as hydroxides when the local pH increases near the cathode during natural seawater electrolysis, which can block the surface of catalyst and lead to decrease of activity and durability. However, in the case of "alkaline nS" (1 M KOH+natural seawater), the Ca^{2+} and Mg^{2+} ions can be pre-deposited and removed by the alkaline solution (1 M KOH). Thus, the influence of $Ca(OH)_2$ and $Mg(OH)_2$ precipitation can be eliminated through the pre-treatment with alkaline solution, and the RuO_2-C-300 catalyst can exhibit a long-term durability in overall seawater splitting.

The characterizations of catalyst after stability test have also been measured. Chemical states of RuO_2-C-300 after HER and OER tests have been investigated by XPS. The Ru 3p spectrum can be split into two peaks for Ru (IV) $3p_{3/2}$ and Ru (IV)$3p_{1/2}$ centered at 463.9 eV and 486.2 eV, respectively (Figure 4c). No obvious peak shift between the RuO_2-C-300 after HER and OER tests, although peak intensity decreased for RuO_2-C-300 after OER test. The O 1s spectrum can be split into three peaks for lattice O, hydroxyl and the C-O-C interaction. The peak intensity for lattice O and C-O-C interaction (from the carbon cloth) of RuO_2-C-300 after OER test increased relative to RuO_2-C-300 after HER, which may be caused by the oxidation potential at anode (Figure 4d). The XRD patterns of RuO_2-C-300 after HER and OER tests clearly show the diffraction peaks at 35.1° and 54.2°, which are correspond to the (101) and (211) planes of RuO_2, respectively, although the diffraction peak of (110) plane has been covered by the strong peak of carbon cloth (Figure 4e). From the XPS and XRD data, it is concluded that the RuO_2-C-300 is very stable for the overall seawater splitting.

The above-mentioned electrolyser was then paired with a commercial Si solar cell to examine its performance in solar-driven overall seawater splitting (Figure 4f). The integrated system demonstrated spontaneous H_2 and O_2 evolution upon simulated solar irradiation (Figure S13, Video S1). As depicted in Figure 4f, the integrated system demonstrated spontaneous H_2 and O_2 evolution at a current density of 40.5 mA cm^{-2}. The Faradaic efficiency of the system in seawater was calculated by dividing the amount of collected gases by theoretical amount of gases from the amount of charge. The RuO_2-C-300 electrodes demonstrated 95% Faraday efficiency with a H_2:O_2 ratio of 2:1 (Table S6, Figure S14, detailed calculation procedure in SI). To verify whether ClO^- ions were produced at anode, the electrolyte after OER stability test was detected by an o-Tolidine indicator test. No adsorption peaks were observed in the UV-vis spectra, which implies no ClO^- ions in the solution [38] (Figure S15).

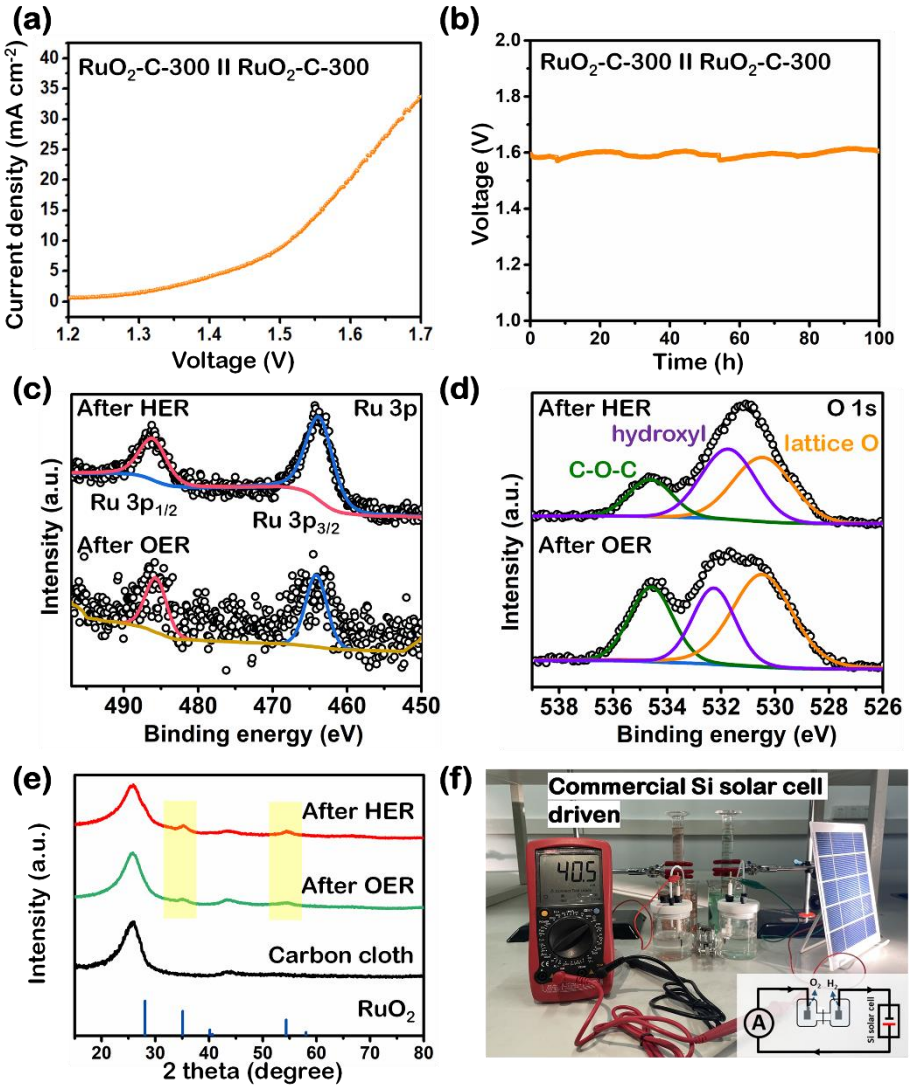

Figure 4. (a) Polarization curve and (b) durability test of RuO_2-C-300 in a two-electrode electrolyzer tested in alkaline nS electrolyte. XPS spectra of (c) Ru 3p and (d) O 1s for RuO_2-C-300 after HER and OER tests. (e) XRD patterns of RuO_2-C-300 after the durability test. (f)

A photo showing a commercial silicon solar cell-driven electrolysis (1 × 1 cm^2 electrodes) of alkaline nS.

We ascribe these remarkable electrocatalytic performances of RuO_2-C-300 to the RuO_2 nanoparticles with interfacial carbon. According to the above-mentioned design and synthesis by controllable calcination, Ru ions in the organic framework, as shown schematically in Figure 5a-left, will be oxidized and sintered to small RuO_2 nanoparticles with low crystallinity, while carbonization of the framework proceeds (Figure 5a-middle). The exposed surface organic ligands can be oxidized to CO_2 gases, which is accompanied by large mass loss and shrinkage of structure. The surface carbon is then oxidized and removed, however, the inner organic ligands surrounded by RuO_2 nanoparticles can be protected against oxidation and carbonized gradually to form amorphous interfacial carbon for restraining grain growth of RuO_2 and stabilizing the RuO_2 nanoparticles (Figure 5a-right). Moreover, the relatively low degree of crystallinity of RuO_2 facilitates a rich coverage of hydroxyl groups, which enhances hydrophilicity.[13,34-36]

For the reactions as expressed in Figure 5b, formation of all Ru-activated intermediates, whether in alkaline, acidic or neutral solution, is strongly dependent on the rate of transport of electrons and strength of adsorption of the reactants. To this end, there are three advantages in RuO_2 with interfacial carbon for efficient electrocatalysis of seawater splitting (figure 5b), involving

i) interfacial carbon forming a unique nanofusion structure for efficiently increasing electronic conduction;

ii) nano-effects and a corresponding high exposure of active sites in RuO_2 nanoparticles confined by interfacial carbon;

iii) high water affinity caused by surface hydroxyl group coverage in low-crystallinity RuO_2 for enhancing contact with reactant water (figure S12).

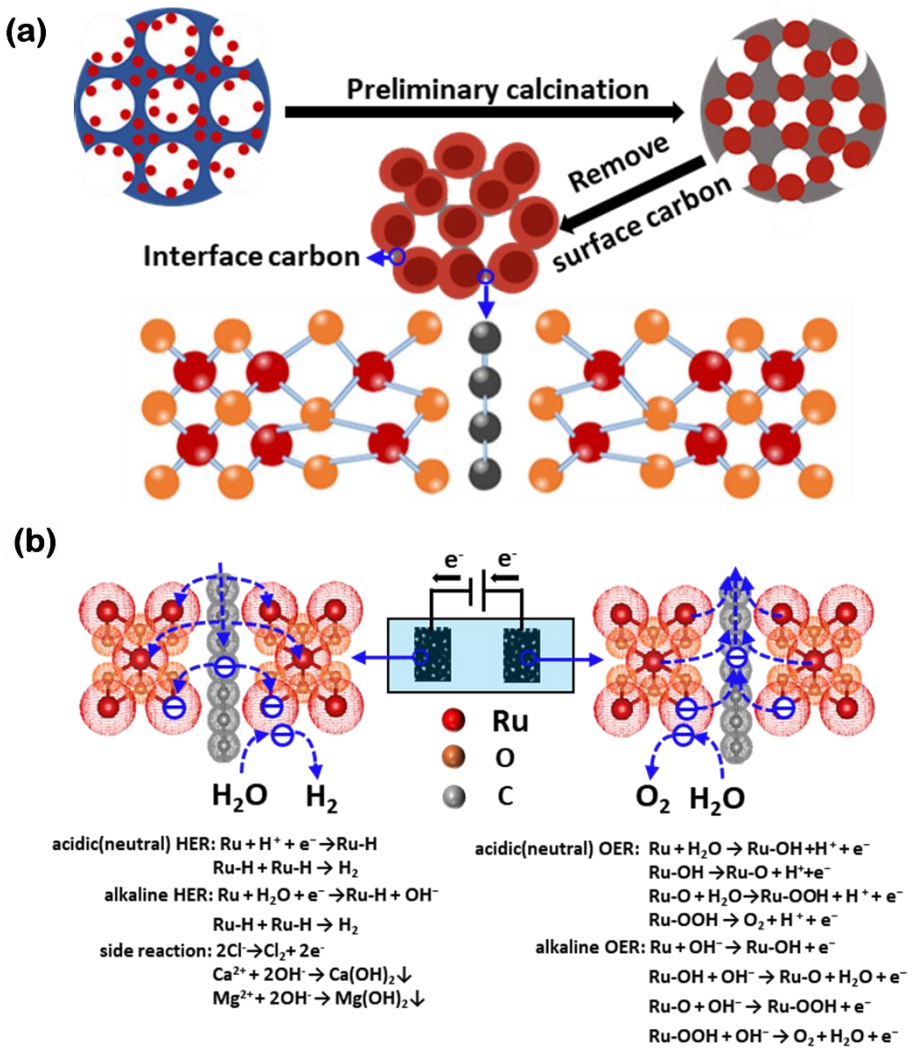

Figure 5. (a) Schematic illustration of RuO_2-C-300 and the merits of interfacial carbon for overall seawater splitting. (b) Schematic of a two-electrode water electrolyzer.

3. Conclusion

A facile and controllable oxidization-calcination strategy has been used to synthesize RuO_2 nanocrystals with interfacial carbon, yielding efficient electrocatalysts without charge transfer limitations between numerous active sites. This unique RuO_2-C structure shows significant advantages for pH-universal electrocatalytic overall seawater splitting, in both simulated and natural seawater. An electrolyze using RuO_2-C was assembled for overall seawater splitting, which outputs current densities of 10 mA cm^{-2} at record low cell voltage of 1.52 V, and shows excellent durability at current densities of 10 mA cm^{-2} for up to 100 h. This work represents a significant and very promising step forward in the development of a robust and active catalyst to utilize the world's abundant seawater feedstock for large-scale hydrogen and oxygen production by renewable energy sources.

4. Experimental Section

Synthesis of the copper benzene-1,3,5-tricarboxilate (Cu-BTC): The octahedral Cu-BTC particles were synthesized according to previous research with some modification.[39] Firstly, 4.6 g of benzene-1,3,5-tricarboxylic acid was dissolved in 500 mL methanol solution. Then 5 g of Cu $(NO_3)_2 \cdot 3H_2O$ and 4.6 g of PVP were dissolved in another 500 mL methanol solution. The latter solution was added to the former solution to form a homogeneous solution by stirring. Then the solution was allowed to settle and kept at room temperature for 24 h. The resultant blue sample powder was obtained by suction filtration and washed with ultrapure water three times before being dried at 60 ℃ for 12 h.

Synthesis of the Ru^{3+}-C: In a typical preparation of Ru^{3+}-C, 1.5 mL of $RuCl_3 \cdot xH_2O$ (0.2 mol L^{-1}) and 120 mg of Cu-BTC powder were dispersed uniformly into 36 mL of methanol through ultrasonic dispersion. Then, the solution was transferred into a Teflon-lined stainless-steel autoclave (50 mL) and maintained at 80 ℃ for 4 h in oven. After cooling to room temperature, the resultant products were collected by centrifugation and washed with ultrapure water three times before being dried at 60 ℃ for 12 h.

Synthesis of the RuO_2-C-T: The Ru^{3+}-C was pyrolyzed at different temperatures (250 ℃, 300 ℃, 350 ℃ and 400 ℃) for 4 h with a heating rate of 5 ℃ min^{-1} under air atmosphere.

Synthesis of the commercial RuO_2/C: The commercial RuO_2/C was prepared by mechanical mixing of commercial RuO_2 (5 mg) and Vulcan XC-72 carbon (1 mg).

Supporting Information

Supporting Information is available from the Wiley Online Library or from the author.

Acknowledgements

Fang Fang, Yong Wang, and Le-Wei Shen contributed equally to this work. This work was supported by National Natural Science Foundation of China (51861135313), Sino-German Centre's COVID-19 Related Bilateral Collaborative project (C-0046), National 111 project (B20002), Program for Changjiang Scholars and Innovative Research Team in University (IRT_15R52), Shenzhen Science and Technology Program (JCYJ20210324142010029, GJHZ20210705143204014), Guangdong Province International Scientific and Technological Cooperation Projects (2020A0505100036), and Guangdong Basic and Applied Basic Research Foundation (2019A1515110435, 2021A1515111131, 2022A1515010137, 2022A1515010504). KIO thanks the NRF (113638) and South Africa's National Research Foundation through the SARChI Chair in Materials Electrochemistry and Energy Technologies

(132739). MDS thanks the Royal Society for a University Research Fellowship (UF150104). DC acknowledge support of the Prime Minister's Fuel-Choice Initiative, within the framework of the "*Israel National Research Center for Electrochemical Propulsion*" (INREP), funded by the Planning & Budgeting Commitee of the Israel Council for Higher Education (CHE). We thank the Nanostructure Research Centre (NRC) for the S/TEM work.

eceived: ((will be filled in by the editorial staff))
Revised: ((will be filled in by the editorial staff))
Published online: ((will be filled in by the editorial staff))

References

[1] X. Wu, S. Zhou, Z. Wang, J. Liu, W. Pei, P. Yang, J. Zhao, J. Qiu, *Adv. Energy Mater.* **2019**, *9*, 1901333.

[2] Y. Yao, X. Gao, X. Meng, *Int. J. Hydrogen Energy* **2021**, *46*, 9087-9100.

[3] Y. Kuang, M. J. Kenney, Y. Meng, W. H. Hung, Y. Liu, J. E. Huang, R. Prasanna, P. Li, Y. Li, L. Wang, M. C. Lin, M. D. McGehee, X. Sun, H. Dai, *Proc. Natl. Acad. Sci.* **2019**, *116*, 6624-6629.

[4] L. Yu, L. Wu, S. Song, B. McElhenny, F. Zhang, S. Chen, Z. Ren, *ACS Energy Lett.* **2020**, *5*, 2681-2689.

[5] S.-H. Hsu, J. Miao, L. Zhang, J. Gao, H. Wang, H. Tao, S.-F. Hung, A. Vasileff, S. Z. Qiao, B. Liu, *Adv. Mater.* **2018**, *30*, 1707261.

[6] L. Yu, Q. Zhu, S. Song, B. McElhenny, D. Wang, C. Wu, Z. Qin, J. Bao, Y. Yu, S. Chen, Z. Ren, *Nat. Commun.* **2019**, *10*, 5106.

[7] S. Higgins, *Nat. Chem.* **2010**, *2*, 1100.

[8] J. Yu, Q. He, G. Yang, W. Zhou, Z. Shao, M. Ni, *ACS Catal.* **2019**, *9*, 9973-10011.

[9] X. Niu, Q. Tang, B. He, P. Yang, *Electrochim. Acta* **2016**, *208*, 180-187.

[10] N. Danilovic, R. Subbaraman, K.-C. Chang, S. H. Chang, Y. J. Kang, J. Snyder, A. P. Paulikas, D. Strmcnik, Y.-T. Kim, D. Myers, V. R. Stamenkovic, N. M. Markovic, *J. Phys. Chem. Lett.* **2014**, *5*, 2474-2478.

[11] H. Ma, C. Liu, J. Liao, Y. Su, X. Xue, W. Xing, *J. Mol. Catal. A: Chem.* **2006**, *247*, 7-13.

[12] T. D. Nguyen, G. G. Scherer, Z. J. Xu, Electrocatalysis 2016, 7, 420; J. Kibsgaard, T. R. Hellstern, S.-J. Choi, B. N. Reinecke, T. F. Jaramillo, *Electrocatalysis* **2016**, *7*, 420-427.

[13] J. Kibsgaard, T. R. Hellstern, S.-J. Choi, B. N. Reinecke, T. F. Jaramillo, *ElectroChem* **2017**, *4*, 2480-2485.

[14] E. Tsuji, A. Imanishi, K.-i. Fukui, Y. Nakato, *Electrochim. Acta* **2011**, *56*, 2009-2016.

[15] A. Grimaud, O. Diaz-Morales, B. Han, W. T. Hong, Y.-L. Lee, L. Giordano, K. A. Stoerzinger, M. T. M. Koper, Y. Shao-Horn, *Nat. Chem.* **2017**, *9*, 457-465.

[16] T. Audichon, T. W. Napporn, C. Canaff, C. Morais, C. Comminges, K. B. Kokoh, *J. Phys. Chem. C* **2016**, *120*, 2562-2573.

[17] R. Kötz, S. Stucki, *Electrochim. Acta* **1986**, *31*, 1311-1316.

[18] Y. Dong, S.-Y. Chen, Y. Lu, Y.-X. Xiao, J. Hu, S.-M. Wu, Z. Deng, G. Tian, G.-G. Chang, J. Li, S. Lenaerts, C. Janiak, X.-Y. Yang, B.-L. Su, *Chem. Asian J.* **2018**, *13*, 1609-1615.

[19] S. Hao, M. Liu, J. Pan, X. Liu, X. Tan, N. Xu, Y. He, L. Lei, X. Zhang, *Nat. Commun.* **2020**, *11*, 5368.

[20] M. Teliska, W. E. O'Grady, D. E. Ramaker, *J. Phys. Chem. B* **2005**, *109*, 8076-8084.

[21] H. Yan, Y. Xie, A. Wu, Z. Cai, L. Wang, C. Tian, X. Zhang, H. Fu, Advanced Materials 2019, 31, 1901174; M. Li, Y. Zhu, H. Wang, C. Wang, N. Pinna, X. Lu, *Adv. Mater.* **2019**, *31*, 1901174.

[22] M. Li, Y. Zhu, H. Wang, C. Wang, N. Pinna, X. Lu, *Adv. Energy Mater.* **2019**, *9*, 1803185.

[23] N.-T. Suen, S.-F. Hung, Q. Quan, N. Zhang, Y.-J. Xu, H. M. Chen, Chemical Society Reviews 2017, 46, 337; B. You, M. T. Tang, C. Tsai, F. Abild-Pedersen, X. Zheng, H. Li, *Chem. Soc. Rev.* **2017**, *46*, 337-365.

[24] B. You, M.-T. Tang, C. Tsai, F. Abild-Pedersen, X. Zheng, H. Li, *Adv. Mater.* **2019**, *31*, 1807001.

[25] a) T. Bhowmik, M. K. Kundu, S. Barman, *ACS Appl. Mater. Interfaces* **2016**, *8*, 28678-28688; b) Z. Ma, Y. Zhang, S. Liu, W. Xu, L. Wu, Y.-C. Hsieh, P. Liu, Y. Zhu, K. Sasaki, J. N. Renner, K. E. Ayers, R. R. Adzic, J. X. Wang, *J. Electroanal. Chem.* **2018**, *819*, 296-305.

[26] Y.-X. Xiao, J. Ying, J.-B. Chen, Y. Dong, X. Yang, G. Tian, J. Wu, C. Janiak, K. I. Ozoemena, and X.-Y. Yang, *Chem. Mater.* **2022**, *34*, 3705-3714.

[27] X. Cui, P. Ren, C. Ma, J. Zhao, R. Chen, S. Chen, N. P. Rajan, H. Li, L. Yu, Z. Tian, D. Deng, *Adv. Mater.* **2020**, *32*, 1908126.

[28] Y. Lu, X.-L. Liu, L. He, Y.-X. Zhang, Z.-Y. Hu, G. Tian, X. Cheng, S.-M. Wu, Y.-Z. Li, X.-H. Yang, L.-Y. Wang, J.-W. Liu, C. Janiak, G.-G. Chang, W.-H. Li, G. Van Tendeloo, X.-Y. Yang, B.-L. Su, *Nano Lett.* **2020**, *20*, 3122-3129.

[29] S.-M. Wu, X.-L. Liu, X.-L. Lian, G. Tian, C. Janiak, Y.-X. Zhang, Y. Lu, H.-Z. Yu, J. Hu, H. Wei, H. Zhao, G.-G. Chang, G. Van Tendeloo, L.-Y. Wang, X.-Y. Yang, B.-L. Su, *Adv. Mater.* **2018**, *30*, 1802173.

[30] D. Lin, Y. Liu, Z. Liang, H.-W. Lee, J. Sun, H. Wang, K. Yan, J. Xie, Y. Cui, *Nat. Nanotech.* **2016**, *11*, 626.

[31] D. Rochefort, P. Dabo, D. Guay, P. M. A. Sherwood, *Electrochim. Acta* **2003**, *48*, 4245-4252.

[32] M. C. Biesinger, B. P. Payne, A. P. Grosvenor, L. W. M. Lau, A. R. Gerson, R. S. C. Smart, *Appl. Surf. Sci.* **2011**, *257*, 2717-2730.

[33] S. Anantharaj, P. E. Karthik, B. Subramanian, S. Kundu, *ACS Catal.* **2016**, *6*, 4660-4672.

[34] S.-S. Fan, L. Shen, Y. Dong, Tian, G., S.-M. Wu, G.-G. Chang, C. Janiak, P. Wei, J.-S. Wu, X.-Y. Yang, *J. Energy Chem.* **2021**, *57*, 189-197.

[35] H.-Z.Yu, Y. Wang, J. Ying, S.-M. Wu, Y. Lu, J. Hu, J.-S. Hu, L. Shen, Y.-X. Xiao, W. Geng, G.-G.Chang, C. Janiak, W.-H. Li, X.-Y. Yang, *ACS Appl. Mater. Interfaces* **2019**, *11*, 27641-27647.

[36] S.-T. Xiao, S.-M. Wu, Y. Dong, J.-W. Liu, L.-Y. Wang, L. Wu, Y.-X. Zhang, G. Tian, C. Janiak, M. Shalom, Y.-T. Wang, Y.-Z. Li, R.-K. Jia, D. W. Bahnemann, X.-Y. Yang, *Chem. Eng. J.* **2020**, *400*, 125909.

[37] O. Delmer, P. Balaya, L. Kienle, J. Maier, *Adv. Mater.* **2008**, *20*, 501-505.

[38] S. H. Hsu, J. Miao, L. Zhang, J. Gao, H. Wang, H. Tao, S. F. Hung, A. Vasileff, S. Z. Qiao, B. Liu, Adv. Mater., 2018, 30, 1707261.

[39] K. A. Stoerzinger, R. R. Rao, X. R. Wang, W. T. Hong, C. M. Rouleau, Y. Shao-Horn, *Chem* **2017**, *2*, 668.